ARTICLE

fib WILEY

Thin-walled concrete beams with stay-in-place flexible formworks and integrated textile shear reinforcement

Minu Lee[1] ⓘ | **Jaime Mata-Falcón**[1] ⓘ | **Mariana Popescu**[2] | **Walter Kaufmann**[1] ⓘ

[1]Institute of Structural Engineering, ETH Zurich, Zurich, Switzerland

[2]Faculty of Civil Engineering and Geosciences, Delft University of Technology (TU Delft), Delft, The Netherlands

Correspondence
Minu Lee, Institute of Structural Engineering, ETH Zurich, Zurich, Switzerland.
Email: mlee@ethz.ch

Abstract

Thin-walled textile-reinforced concrete beams have recently emerged as a promising approach for material-efficient design. However, the increased complexity of the formwork is a major challenge in implementing such elements for broader use in the construction industry. This study presents a novel type of stay-in-place flexible formworks with integrated textile reinforcement. The use of weft-knitted textiles allows the integration of continuous high-strength rovings as shear reinforcement and the introduction of spatial features within the fabric to guide bending-active rods to shape the complex cross-section geometry. The manufacturing procedure and the structural performance were investigated in an experimental campaign consisting of four concrete beams with I-profile cross sections tested in three-point bending, where aramid rovings were used for the shear and conventional deformed steel bars for the flexural reinforcement. The transverse reinforcement ratio proved to be essential in increasing the shear strength. Thereby, the use of digital image correlation measurements of the surface deformations allowed the direct assessment of the strains and, thus, the mechanical activation of the textile reinforcement. The full tensile capacity of all the aramid rovings crossing the governing crack could not be exploited due to the brittle material behavior, resulting in a progressive failure once the first roving reached its tensile strength. Compatibility-based stress fields were used to predict the load-deformation and failure behavior of the tested beams, which resulted in an excellent agreement of the ultimate loads and failure modes obtained from the model with the observations and results from the experiments.

KEYWORDS
crack behavior, digital image correlation, experimental study, KnitCrete, lightweight concrete structures, shear, textile-reinforced concrete

1 | INTRODUCTION

The geometrical optimization of concrete elements has always been a fundamental part of the design philosophy in concrete construction, which is not only represented in complex solutions such as ribbed slabs or vaulted shells but also in widespread applications such as hollow box bridge girders. More recently, the reduction of the

concrete volume used in construction triggered by sustainability demands has become one of the critical drivers for the development of new composite materials and structural typologies. Thereby, thin-walled concrete beams with T-profile or I-profile sections using textile reinforcement have emerged as an extension of the design spectrum of concrete structures with small to medium spans, as highlighted in recent research in the literature (e.g.,[1–3]). The use of noncorrosive materials for the reinforcement allows to reduce the total element thicknesses to a few centimeters since no minimum concrete cover has to be provided (typically between 20 and 60 mm depending on the building codes and exposure). Textile reinforcement typically consists of bundles of filaments ("rovings") of high-strength materials, such as aramid, carbon, and glass fibers, which are arranged in a bi-directional grid.[4] The rovings are usually coated or even fully impregnated with a resin (e.g., epoxy) to increase their robustness against lateral loading[5] and to improve the interfiber friction between individual filaments for a more homogeneous stress distribution over the roving section.[6] While textile–concrete composites present an efficient approach for reducing material consumption, the increased cost and labor due to the higher degree of formwork complexity presents a major challenge for a broad application in the construction sector. Fabric formworks make use of flexible membranes as concrete molds, which might simplify the construction of concrete elements with nonstandard geometries. Recent studies in the literature have investigated various structural elements, including columns, beams, slabs, and shells (e.g.,[7–9]). Due to the low flexural stiffness of the fabrics (in contrast to conventional formwork typically made from stiff wood or steel panels), the formwork exhibits large deformations caused by the hydrostatic pressure from the wet concrete,[10] making it more difficult to achieve high geometrical precision in the final structure. The KnitCrete technology developed at ETH Zurich[11,12] is a stay-in-place flexible formwork system that provides higher stiffness and strength during construction by applying a thin layer of either fast-setting cement paste or epoxy resin after tensioning the fabrics in a scaffolding frame. Bending-active rods or cables may be integrated within the textile as additional supports. While the feasibility of the construction procedure on an architectural scale was highlighted in the KnitCandela pavilion,[13] the type and placing of reinforcement for structures built with this technology have not been solved yet. Several previous studies focused on the mechanical behavior of stay-in-place flexible formworks with integrated textile reinforcement for thin membrane elements in uniaxial tension and slender slab strips in bending,[14–16] showing a beneficial postcracking behavior.

The authors revised various potential reinforcement strategies in Ref. [17], concluding that (i) ensuring structural integrity only with textile reinforcement is challenging, but (ii) the integration of continuous high-strength fiber materials in the stay-in-place formwork offers the potential for an efficient structural design while maintaining the advantages of the fast construction procedure. Based on these findings, the authors investigated the use of tubular textiles for linear bending beams with integrated high-strength aramid inlays winding around the circumference of the rectangular cross section and acting as shear reinforcement, while the bending resistance was provided by conventional deformed steel bars.[18] The present study explores the further optimization of the cross-section geometry with a thin-walled I-profile cross section manufactured using weft-knitted textiles where the stirrups are integrated within the web and are fully anchored, winding around the longitudinal reinforcement. An experimental campaign consisting of four beams with different transverse reinforcement ratios was conducted to study the structural behavior and the failure modes. The mechanical activation of the textile reinforcement was assessed based on digital image correlation (DIC) measurements. Furthermore, numerical simulations using compatibility-based stress fields were used to predict the load-deformation behavior and the shear strength of the examined beams.

2 | CONCEPTUAL DESIGN AND MANUFACTURING PRINCIPLES

The integration of reinforcement within the formwork leads to various requirements on the manufacturing technology. While the ease of use—regarding the installation of the textile, the placing of the reinforcement, and the concrete casting—is the major criterion during construction, the textile reinforcement needs to be properly anchored to ensure its mechanical activation under the intended loading conditions in the final state. This section investigates the design of structures using such a combined formwork and reinforcement system while considering both the technical feasibility of manufacturing the fabric and the mechanical characteristics of continuous high-strength fibers to achieve a beneficial structural behavior.

While the fibrous materials typically used for textile reinforcement (e.g., aramid, carbon, or glass fibers) present many advantages, such as the robustness against environmental influences (except UV) and the high strength at moderate to high stiffness, the brittle failure behavior—i.e., the rovings progressively fail once the first filament reaches its tensile strength—challenges the established design principles for conventional reinforced

concrete structures, which rely on the internal redistribution of forces and large deformation capacity of the used materials and elements to achieve a robust behavior. The lack of ductility in typical textile reinforcement materials and their sensitivity to nonaxial loading leads to a large scatter in determining their strength and differences between the nominal values and the resistance observed in experimental testing. While the strength can be adjusted using reduction factors as suggested in several studies in the literature (e.g.,[5,19,20]), and the scatter of the material properties is related to the safety format as investigated in Refs. [21,22], the inherent challenges of a sudden collapse prevail when the structure only relies on materials that do not exhibit ductile behavior. A brittle behavior was observed in most studies on conventional textile-reinforced concrete members for thin-walled elements in the literature,[1,2,20,23] where besides the rupture of the textile reinforcement, premature spalling of the concrete cover in the web and splitting cracks in the flanges were the predominant causes for failure.

In a previous study,[18] the authors investigated the fabrication and the structural behavior of concrete beams made from tubular fabrics where continuous aramid rovings were integrated within the textile. Most specimens exhibited a sudden failure in shear once the peak load was reached. However, the use of deformed steel bars in the tension chord provided a large deformation capacity given that the transverse textile reinforcement could sustain the shear force until the beam failed in bending due to the rupture of the flexural reinforcement. The activation of the textile reinforcement in shear, i.e., assuming the role of stirrups in conventional reinforced concrete beams, could be directly measured using DIC, which revealed a substantial debonding of the textile from the concrete, emphasizing the importance of the proper mechanical anchorage of the "stirrups." While tubular textiles allow a wide range of feasible cross-section types, one major disadvantage is the need to cast the specimens upright since the openings of the textiles are located at the ends of the beam, which limits the feasible spans due to the formwork pressure exerted by the wet concrete. Possible solutions to prevent large deformations or even failure of the formwork include set-on-demand concrete processes as used in other construction technologies, enabled by using ultra-thin formworks,[24,25] or holes in the textiles to fill the concrete in a horizontal position, whose feasibility depends on the roving spacing.

This study explores an alternative method where the cross section can be formed by folding a flat textile into the desired shape, with cables or bending-active rods defining the vertices, and being tensioned using ropes in a scaffolding frame. In contrast to tubular textiles, one side of the cross section is left open (as shown in Figure 1a), allowing the concrete to be cast with the beam in a horizontal position. The inlays are only integrated into the straight part of the web and form a loop around the longitudinal reinforcing bars in the tension and compression flange (Figure 1b). The direct connection of the textile roving around the longitudinal reinforcement ensures proper anchorage. Furthermore, it fixes the position of the reinforcing bars as an integral part of the textile, considerably simplifying the placing of the reinforcement during construction.

3 | EXPERIMENTAL PROGRAM

The feasibility of the fabrication processes was validated by manufacturing four concrete beams with thin-walled I-profile cross sections using stay-in-place formworks with integrated textile reinforcement, which were tested to failure in three-point bending. The structural behavior was investigated regarding the applied loads and the measured deformations based on DIC.

3.1 | Specimens, materials, and manufacturing

All specimens were manufactured and tested in the Structures Laboratory at ETH Zurich. Table 1 summarizes the specimen configurations, whereby the inlay spacings varied between 12 and 50 mm, and one specimen did not contain any transverse reinforcement.

3.1.1 | Textiles

The textile formwork was produced in one piece using a gauge 7 CNC flat-bed knitting machine (Steiger Libra 3.130). The knitting was done in the length direction of the beam, with the sectional perimeter (outline) of the beam representing the weft direction of knitting. Two polyester yarns (PES 167 t 30/2) were used to create a sheet of textile that includes longitudinal channels for the insertion of shaping rods, as described in Section 2. Straight inlay aramid yarns were automatically placed during the production process in weft direction, having the correct length and spacing. These inlays formed two continuous zig-zags side-by-side along the length of the textile, thus, connecting the longitudinal reinforcement in the bottom and top flanges of the cross section, which was inserted into these zig-zags (Figure 1b).

As concluded in the authors' previous studies on the mechanical behavior of weft-knitted textile-reinforced concrete,[14–16,18] aramid rovings with a fineness of 800 tex (1 tex = 1 g/km of yarn) were chosen for the inlays since

FIGURE 1 Thin-walled concrete beams from folded textiles: (a) cross section (in upside-down casting position); (b) flat textiles before tensioning with integrated flexural and textile reinforcement, and shaping elements.

TABLE 1 Specimen configurations: dimensions (nomenclature defined in Figure 3a), inlay spacing (s), tension chord reinforcing bar diameter ($\varnothing_s$), and concrete mix batches.

Specimen	b_{inf} (mm)	t_{inf} (mm)	t_w (mm)	b_{sup} (mm)	t_{sup} (mm)	h (mm)	d (mm)	s (mm)	$\varnothing_s$ (mm)	Concrete batch
ISB-T	114.5	57.5	31.3	112.5	57.5	292.5	263.0	—	20	i
ISB-A-s50	120.0	58.0	30.3	117.5	56.0	294.0	268.5	50		ii
ISB-A-s20	113.5	55.5	32.0	118.5	53.0	294.5	262.5	20		iii
ISB-A-s12	122.0	56.0	32.0	120.5	56.5	304.5	269.0	12		i

they exhibited the highest utilization of the material strength and the most convenient handling in the knitting procedure. The inlays had spacings of 50, 20, and 12 mm (as denoted in the specimen nomenclature in Table 1). In the specimen without transverse reinforcement ("ISB-T"), a nonstructural "dummy" yarn at a spacing of 50 mm was used to fix the position of the longitudinal reinforcing bars, as described in Section 2. The textiles were coated with a low-viscous two-component epoxy resin,[26] which was left to cure for at least 24 h at room temperature before casting. The material properties of the high-strength inlays were determined in uniaxial tension tests on coated aramid rovings, as described in Ref. [14], which yielded the mean values for the tensile strength of $f_u = 2583$ MPa and for the Young's modulus of $E_t = 112$ GPa.

3.1.2 | Steel reinforcing bars

The longitudinal reinforcement in the tension and the compression chords consisted of deformed steel bars with

TABLE 2 Young's modulus (E_s), yield (f_{sy}), ultimate strength (f_{su}), and strain at rupture (ε_{su}) of steel reinforcing bars.

Batch	E_s (GPa)	f_{sy} (MPa)	f_{su} (MPa)	ε_{su} (‰)
Ø08	168.1	676.1	797.3	55.0
Ø20	174.7	701.9	889.2	68.9

enhanced corrosion resistance, which exhibit high strength and adequate ductility. The layout of the longitudinal reinforcement consisted of two steel bars with a diameter of Ø20 mm in the tension and Ø8 mm in the compression chord for all specimens. The material properties were determined on bare bars from the same batch in separate uniaxial tension tests, whose results are summarized in Table 2.

3.1.3 | Bending-active glass fiber rods

The elements to shape the cross section geometry consisted of solid round bending-active rods with a diameter

TABLE 3 Young's modulus (E_c), cylinder compressive strength ($f_{c,cyl}$), and tensile strength (f_{ct}) of the different concrete batches.

Batch	E_c (GPa)	$f_{c,cyl}$ (MPa)	f_{ct} (MPa)
i[a]	37.1	73.0	5.6
ii[b]	33.7	61.3	4.9
iii[b]	36.9	67.2	5.0

[a]Ready-mix concrete from local supplier.
[b]Self-consolidating concrete premix.

of Ø10 mm, which were made from unidirectional glass fiber rovings impregnated with a polyester resin (GFRP). The notional tensile strength and Young's modulus specified by the manufacturer were 700 MPa and 33 GPa, respectively.

3.1.4 | Concrete

All specimens were cast with self-consolidating concrete with a maximum aggregate size of 8 mm, which was either prepared in the laboratory using commercially available premixed concrete or delivered from a local ready-mix concrete supplier, resulting in three different batches. The Young's modulus and the uniaxial compression strength were obtained from three standard cylinders with a diameter of 150 mm and a height of 300 mm per batch. The tensile strength was determined from double punch tests[27] on two cylinders with a diameter of 150 mm and a height of 150 mm per batch. The material properties of the concrete were determined on the day of the three-point bending tests, as summarized in Table 3.

3.1.5 | Manufacturing of the specimens

The manufacturing procedure generally followed the principles introduced in Section 2, tensioning the textile in a scaffolding frame as illustrated in Figure 2a. The steel reinforcing bars and the GFRP rods were threaded through the loops created by the inlays and the channels within the textile, respectively, while lying flat on the ground, as shown in Figure 2b. The longitudinal bars and the rods were then fixed at the end plates of the scaffold. The beams were cast upside down with the main flexural reinforcement (steel bars with Ø20 mm) in the upper flange. This creates more space in the geometrically tight conditions of the lower flange (given that the steel bars in the compression chord had a lower diameter) and ensures the proper flow and distribution of the concrete within the formwork, but required the specimens to be flipped before testing. The textile was tensioned in the wooden framework using ropes to maintain the shape of the cross section and the position of the reinforcing bars over the length of the beam (Figure 2c). The epoxy coating was applied on the textile using paint brushes while the formwork was suspended in the frame. After the coating had hardened, the bottom ropes were cutoff, and a temporary wooden pedestal to support the formwork from the bottom was inserted. The concrete was cast from the top side along the whole length of the beam. At the supports and the point of load application, concrete diaphragms, as illustrated in Figure 3, were cast using conventional formwork, and the surface was leveled with local epoxy beds.

Comparing the nominal (illustrated in Figure 3a) with the actual measured (summarized in Table 1) cross-section dimensions reveals some deviations, which were caused by the deformations of the formwork during casting and the manual tensioning procedure. However, the latter is expected to be a minor issue when implemented in a more industrialized production line, where robotic tensioning devices ensure a higher accuracy and can be automatically controlled considering the nonlinear stretching behavior of the textile.

3.2 | Test setup

All beams were tested in three-point bending with a total span of 2000 mm and shear spans of 810 and 1190 mm, as illustrated in Figure 3b. The asymmetric setup led to shear slendernesses (a/d) of 3 and 4.4, resulting in a 47% larger shear force in the shorter span than in the longer one. The supports consisted of rocker bearings, where one end was resting on a PTFE sheet to allow a free horizontal movement. The load was applied through a steel plate connected to the actuator via a spherical bearing. The load was manually controlled using a hydraulic hand pump, which resulted in a loading rate of ∼6 kN/min. Every beam was tested twice: once failure had occurred in a first monotonic loading cycle, the specimen was unloaded, and the broken span was transversally reinforced using prestressing tendons, as shown in Figure 3b. The specimen was then subjected to a second loading cycle until failure.

3.3 | Instrumentation

The applied load was directly measured from the load cell between the actuator and the steel plate at the load introduction. The surface deformations over one full side face of the beam were assessed using 3D-DIC. A pair of ProSilica GT 6600 cameras (6576 × 4384 pixels) with lenses of 28 mm focal length (Zeiss) at a stereo angle of ∼25° covered the field of view of ∼2300 mm in width,
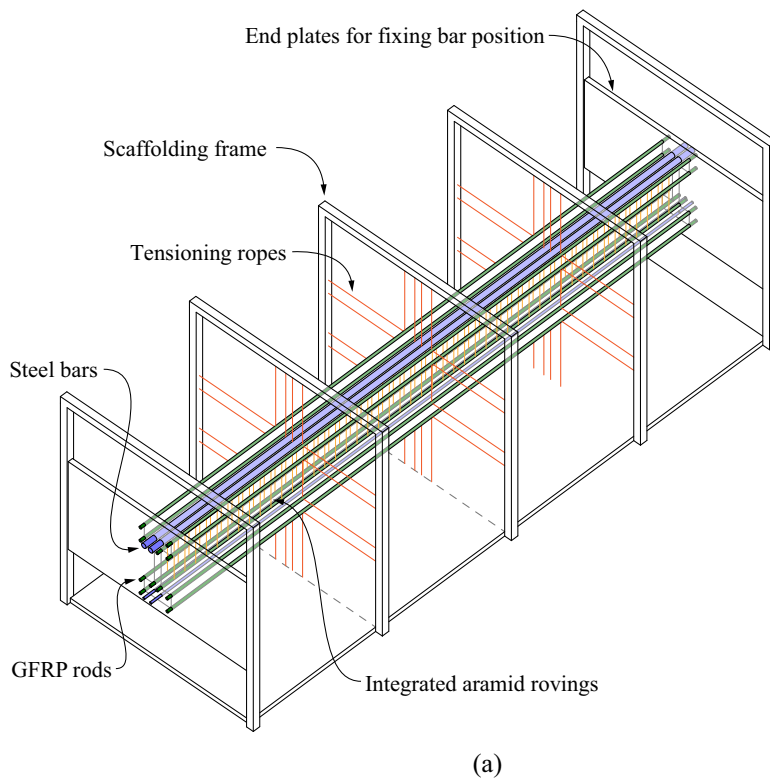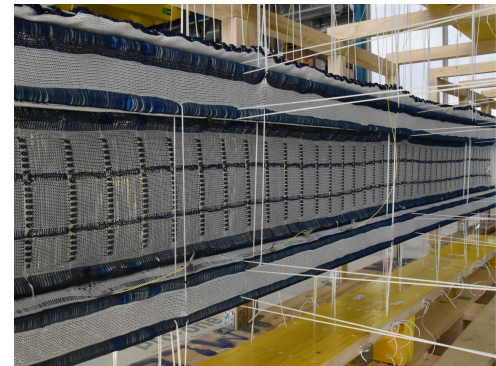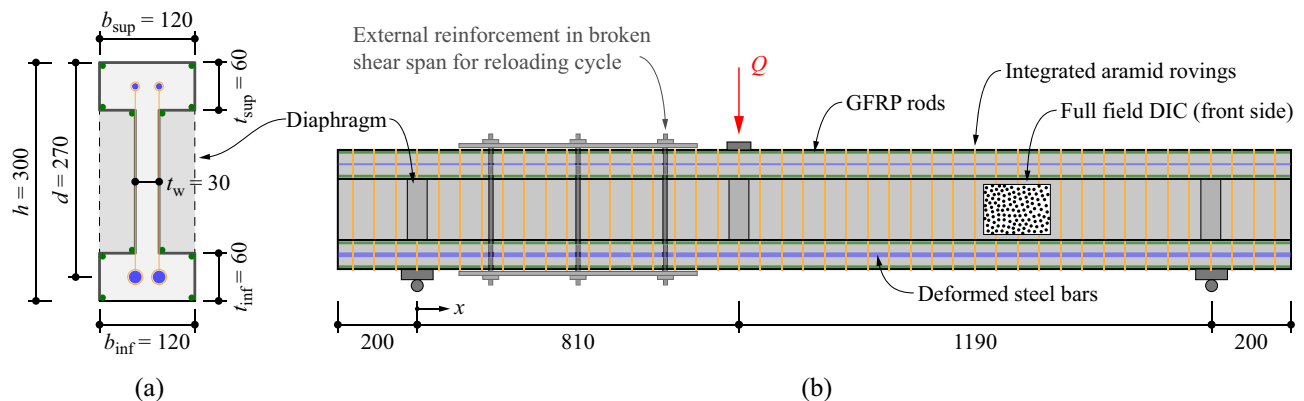
FIGURE 2 Manufacturing of thin-walled concrete beams with stay-in-place formworks and integrated textile reinforcement: (a) scaffolding frame and assembly, (b) textile before tensioning with deformed steel bars and GFRP rods threaded in inlay loops and channels within the fabric, respectively, and (c) tensioning of textile within frame.


FIGURE 3 Specimen configuration: (a) cross-section dimensions, (b) test setup and instrumentation (dimensions in [mm]).

resulting in a resolution of 2.9 pixels/mm. A random dark speckle pattern was applied onto the white-painted specimen using a stiff brush to achieve maximum contrast, thus, improving the correlation. The correlation was performed with the commercial software "VIC-3D" (Correlated Solutions Inc.[28]). The measurement uncertainty was determined with the zero displacement test following,[29,30] which resulted in an average noise level of $\sigma(U, V) = 6 \times 10^{-3}$ mm and $\sigma(\varepsilon_1, \varepsilon_2) = 300$ με, using the following correlation parameters: subset size = 19 pixels,

step size = 5 pixels, and strain filter size = 9. The crack pattern and kinematics on the surface of the beams were analyzed with the open-source software "Automated Crack Detection and Measurement" (ACDM)[31,32] based on the quasicontinuous displacement and strain fields from the DIC measurements. Note that the measurements of the cracks on the surface of the specimens correspond to the deformations in the textile. The crack kinematics in the concrete could not be directly assessed due to the slip between the textile and the concrete
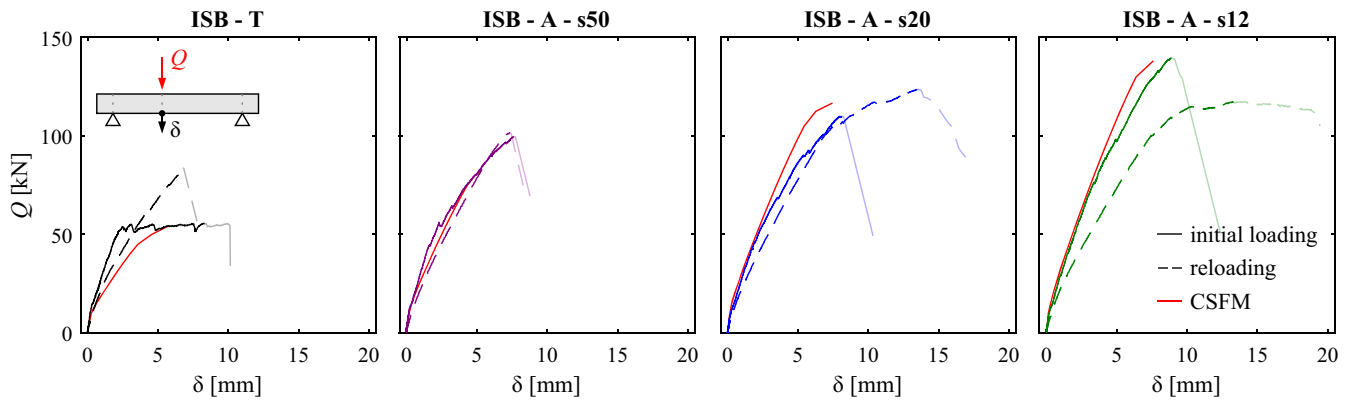
FIGURE 4 Load–deflection relationship of concrete beams with thin-walled I-profile sections: experimental results and predictions based on Compatible Stress Field Method (CSFM) assuming nominal dimensions.

surface, whose implications on the assessment of the crack behavior were reported in Ref. [18] and are described in Section 4.3.

4 | EXPERIMENTAL RESULTS AND DISCUSSION

The structural performance of the specimens was examined regarding the global displacements of the beams, the observed failure modes, and the surface deformations of the textile measured with DIC, which allows characterizing the influences of the high-strength aramid rovings and the concrete on the mechanical behavior of thin-walled concrete beams. A particular focus was on the mechanical activation of the transverse textile reinforcement as the key parameter for increasing the shear strength. The findings from the previous study on the concrete beams with tubular textiles[18] concluded that the estimation of the concrete contribution to the shear transfer across the governing crack essentially relies on the exact measurements of the crack pattern and kinematics, which cannot be directly assessed using DIC due to the presence of the stay-in-place formwork, as discussed in Sections 4.3 and 4.4. However, this contribution is expected to have a minor influence in this study due to the relatively large crack openings,[18] the slender dimensions of the web[20], and the moderate shear slenderness ($a/d \geq 3$).[33]

4.1 | Load-deformation behavior and failure modes

Figure 4 shows the load–deflection relationship of the tested beams, where the initial loading cycle is drawn as a solid and the reloading cycle after reinforcing the

broken span as a dashed line. While the flexural response of most specimens generally exhibited a fairly linear post-cracking behavior and a slight decrease in the stiffness before reaching failure, Specimen "ISB-T" exhibited substantial deflections without an increase of the load in its initial loading cycle. While such behavior might suggest a ductile, hence, benign behavior, it was apparent—already from visual observations during the experiments, as shown in Figure 5a, that a distinct shear crack had formed in the short span, and the sustained load was presumably carried by crack sliding until the diagonal crack abruptly opened, leading to collapse. Note that the strains illustrated in Figure 5a, measured on the textile, correspond to the crack kinematics smeared by local debonding of the textile from the concrete.

All beams with high-strength inlays exhibited a sudden drop of the applied force and rupture of the aramid rovings when reaching the ultimate load (Figure 5b) in the first loading cycle. The shear cracks, which formed as expected in the shorter span, propagated to the flanges, causing horizontal cracks at the web–flange interface and in the compression chord, as shown in Figure 5c,d. The failure loads increased with the transverse reinforcement ratio, as shown in Figure 6, highlighting the significant beneficial influence of the aramid inlays on the shear strength.

When reloading the specimens after strengthening of the short shear span, only the beams without high-strength inlays and with an aramid roving spacing of 50 mm exhibited a shear failure in the longer span. Specimen "ISB-T" reached a higher total load, corresponding to the same shear force in the long shear span as attained in the short shear span in the initial loading cycle (see Table 4). However, Specimen "ISB-A-s50" only reached approximately the same failure load, corresponding to a lower shear resistance in the longer span. The damages that the concrete and the textiles experienced during the
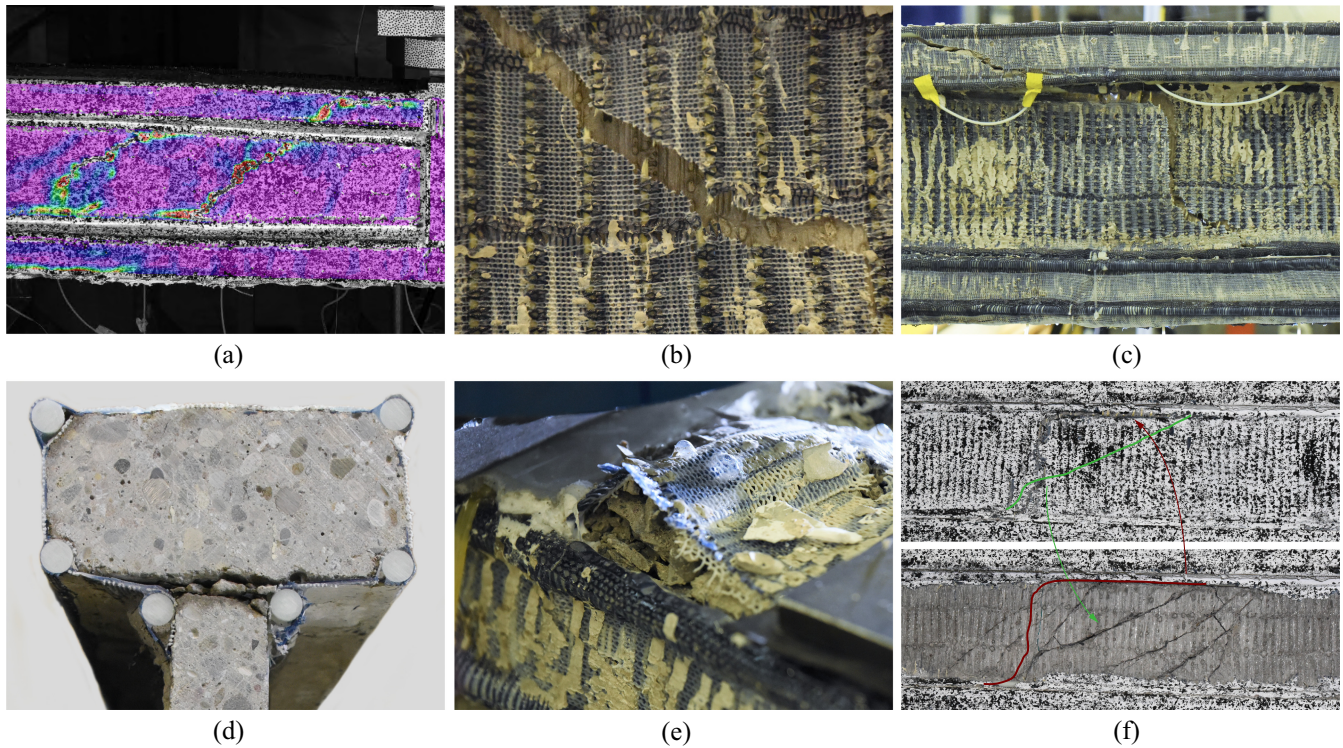
FIGURE 5 Crack and failure behavior of tested concrete beams: (a) substantial crack in textile of Specimen "ISB-T" before failure (illustrated by the measured principal tensile strain field); (b) ruptured aramid rovings in "ISB-A-s20"; (c) propagation of shear crack along web–flange interface and into compression chord; (d) cut specimen after testing ("ISB-T"); (e) concrete crushing in compression chord; (f) governing crack in the concrete (green) and failure crack in textile (red) after testing.
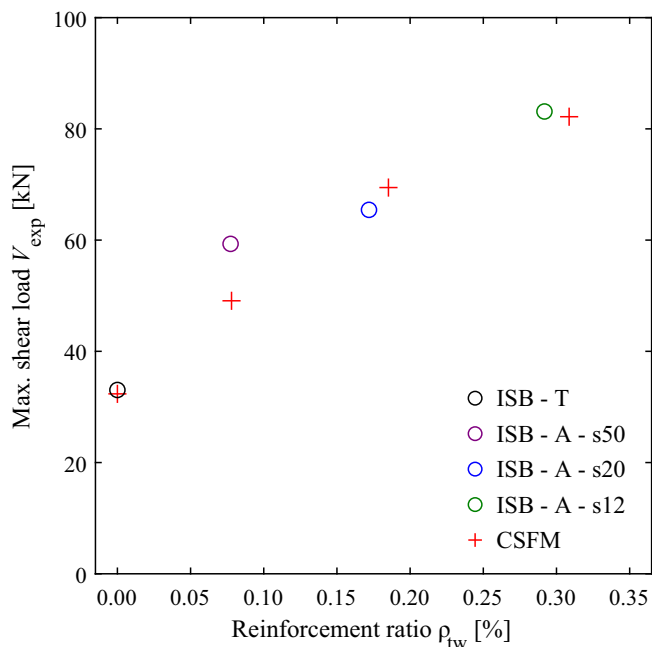
FIGURE 6 Shear force in short shear span at failure versus transverse reinforcement ratio ρ_{tw} under initial loading: experimental values (circles) and predictions based on Compatible Stress Field Method (CSFM) assuming nominal dimensions (crosses).

initial loading cycle and failure of the short span are challenging to assess, which might explain the lower peak load of this specimen in the reloading cycle. Specimens "ISB-A-s20" and "ISB-A-s12" exhibited failure due to the crushing of the concrete in the compression zone (see Figure 5e), reaching higher and lower failure loads at reloading than under initial loading, respectively. The structural integrity of the compression chord in Specimen "ISB-A-s12" was already compromised due to the cracks in the flanges caused by the failure in the initial loading cycle and is, thus, presumably not representative of the actual resistance.

## 4.2 | Behavior of the tension chord and contribution from GFRP rods

The deformations in the tension chord were assessed based on the DIC measurements following the methodology presented in,[15] and adjusted in Ref. [18] The mean strains of the steel bars (ε_{sm}) were determined from the slope obtained from linear regression on the horizontal displacements of the beam at the depth of the reinforcement in the region where the bending moment exceeded 80% of the maximum value. The depth of the

TABLE 4 Shear force in shorter span at failure observed in experiment (V_{exp}), contributions from the textile reinforcement to the shear strength based on digital image correlation measurements (V_{tw}) and theoretical maximum shear resistance provided by the textile reinforcement ($V_{tw,nom}$), predictions based on Compatible Stress Field Method (V_{CSFM}) under initial loading, and in shear force at failure in longer span under reloading ($V_{exp,RL}$).

Specimen	V_{exp} (kN)	V_{tw} (kN)	V_{tw}/V_{exp} (−)	$V_{tw,nom}$ (kN)	V_{CSFM} (kN)	V_{CSFM}/V_{exp} (−)	$V_{exp,RL}$ (kN)
ISB-T	33.1	—	—	—	32.4	0.98	33.9
ISB-A-s50	59.3	20.6	0.35	31.0	49.1	0.83	41.3
ISB-A-s20	65.4	39.9	0.61	78.3	69.5	1.06	50.1
ISB-A-s12	83.1	70.6	0.85	107.1	82.2	0.99	47.6

Note: V_{tw} and $V_{tw,nom}$ correspond to the sum of the vertical forces (determined from the measured strains) and tensile resistances, respectively, of the inlays activated in the stress field, as described in Section 4.3.
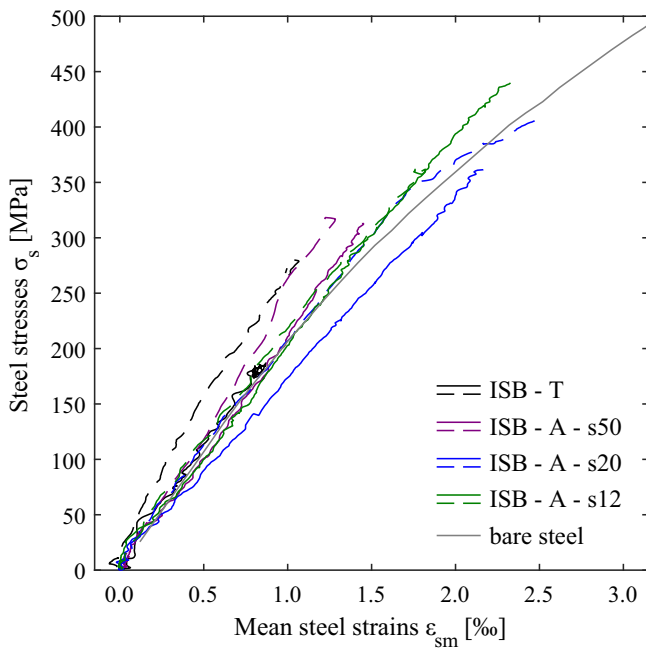
FIGURE 7 Stress–strain relationship of the steel reinforcement in the tension chord compared with bare steel.

compression zone was estimated from the crack tip obtained when applying linear regression on the opening of the bending cracks in the proximity of the maximum bending moment at 70% of the ultimate load obtained by applying ACDM on the surface deformations of the textile as described in Section 3.3.

The mechanical activation of the GFRP rods depends on the bond conditions, which are difficult to assess since the rods are essentially glued by the epoxy coating within the channel of the textile and are not in direct contact with the concrete, as seen in the cut cross section of Specimen "ISB-T" after testing in Figure 5d. Therefore, the contribution of the GFRP rods in the tension chord to the flexural response was deemed to be ineffective and was, therefore, neglected in this study (note that the assumption of a full activation of all six rods in the lower flange

would have only contributed to roughly 10% of the bending moment at ultimate load). The stresses in the steel reinforcement (σ_s) were then determined by applying equilibrium on the cracked cross section.

Figure 7 shows the resulting stress–strain relationship of the steel reinforcing bars in the tension chord. The tensioning stiffening effect from the interaction of the longitudinal reinforcement with the surrounding concrete was practically zero as most specimens closely followed the behavior of the bare steel obtained from the material tests, as described in Section 3.1.2. Specimen "ISB-A-s20" displayed even larger strains than the bare steel at the same stresses, but the stiffness for loads close to failure coincided fairly well. This suggests some unwanted slip due to insufficient bond and anchorage at lower load levels until the reinforcement was properly activated. The reloaded specimens exhibited some peculiar behavior while approaching the ultimate load, such as the sudden change of the stiffness as in Specimen "ISB-A-s20," which presumably originated from the failure of the flexural compression zone. Specimen "ISB-T" exhibited a stagnation of both stresses and strains close to the ultimate load, which underlines that the large deformations observed in Figure 4 were indeed not the result of plastic deformations in the tension chord but were rather caused by the substantial crack sliding, as described in Sections 4.1 and 4.4.

4.3 | Mechanical activation of the textile reinforcement and contribution to the shear strength

As the stay-in-place formwork enclosed the surface of the concrete beams, the measurements from DIC could directly assess the displacements and strains of the textile reinforcement. However, the assessment of the crack pattern and kinematics is subject to higher uncertainty, as described in Ref. [18]. The textile debonded from the
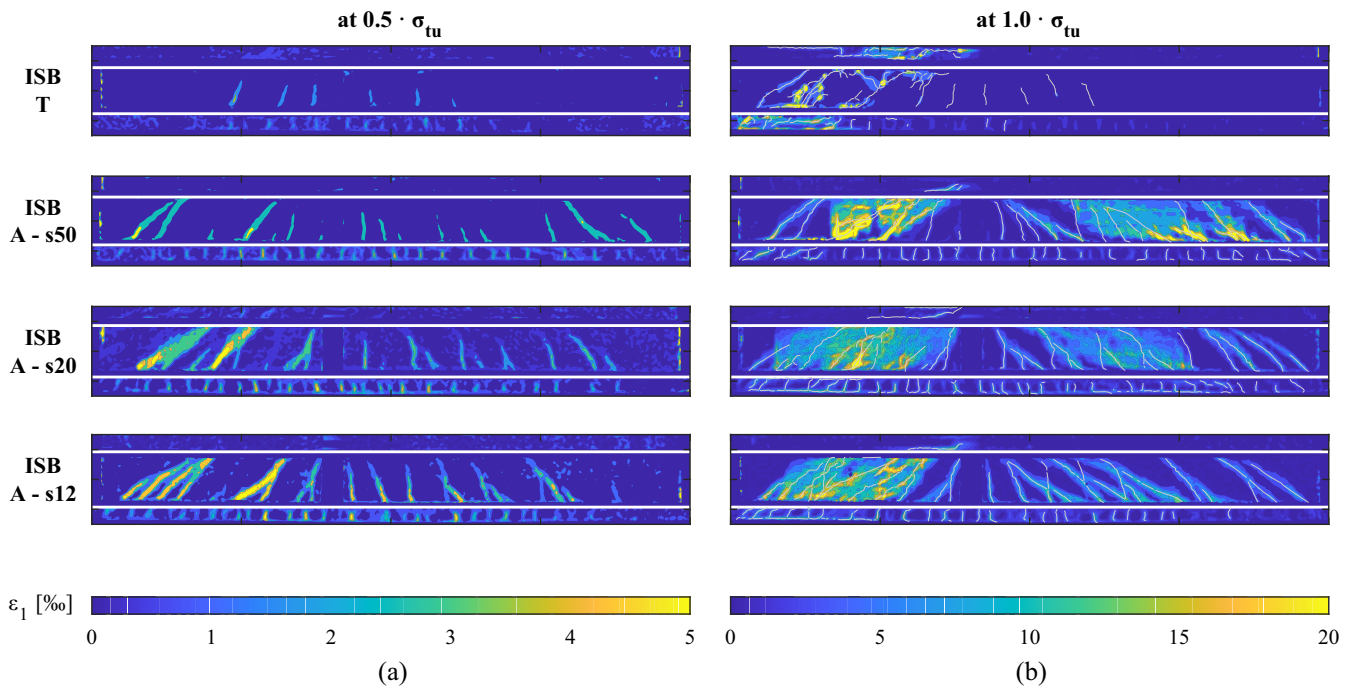
FIGURE 8 Principal tensile strains (ε_1) on the surface of the beams for the initial loading cycle at (a) 50% and (b) 100% of the ultimate load and cracks determined at initial formation (denoted as gray lines).

concrete with increasing crack opening due to the low bond shear stresses between the textile and the concrete, which depend solely on friction and adhesion. The cracks typically—but not necessarily—were distinguishable at initial crack formation, as shown in Figure 8a, which shows the principal tensile strains (ε_1) on the surface of the beams at 50% of the ultimate load of the initial loading cycle. The locations of the cracks in the textile (denoted as gray lines in Figure 8b) were determined at their initial formation using ACDM. The debonding of the textile at higher load levels led to substantial smearing of the strains over the height of the web for the specimens with high-strength inlays, which is generally beneficial for the strength and deformation capacity of the aramid inlays since the deformations are being spread over a larger region instead of being concentrated in the vicinity of the cracks as in stirrups fully embedded in the concrete (as described in Ref. [18]), but made it impossible to distinguish individual cracks. Specimen "ISB-T" (without any aramid rovings) did not exhibit this behavior since the epoxy-coated base textile had ruptured before the failure since the shear strength was presumably mainly provided by the concrete.

The contribution of the textile reinforcement to the shear strength was determined from the strains in the vertical direction (ε_{yy}) measured with DIC. Figure 9 shows the strain distribution in the textile of the specimens with high-strength inlays and the representative values (ε_{tw}, determined as 95%-quantile of the strains at

every section) along the span at ultimate load. The tensile capacity of the transverse textile reinforcement was not fully exploited as the strains reached the ultimate value ($\varepsilon_{tu} = f_{tu}/E_t$) only in limited regions, where the failure crack in the textile would eventually be initiated. Specimen "ISB-A-s50" locally exceeded the failure strain, which, however, occurred mostly between two adjacent inlays where the epoxy-coated base textile had ruptured prior to collapse, whereby the exceedance of the strains in some rovings was within the scatter of the material properties. The strain field measurements in the web suggest the activation of the transverse reinforcement by a load suspension mechanism modeled as a discontinuous stress field, as illustrated in Figure 10a. The shear strength provided by the aramid rovings (V_{tw}) was, thus, determined from

$$V_{tw} = \sum_{i}^{n_{rov}} \varepsilon_{tw,i} \cdot E_t \cdot A_{rov} \tag{1}$$

where $\varepsilon_{tw,i}$, representative strain in one roving activated in the stress field(denoted as red dots in Figure 9); A_{rov}, cross-sectional area of one roving; n_{rov}, number of rovings activated in the stress field (denoted as gray lines in Figure 9). It was assumed that the strains in the rovings were the same on both sides of the web since there were no measurements available from the back side of the specimen. Table 4 summarizes the resulting forces
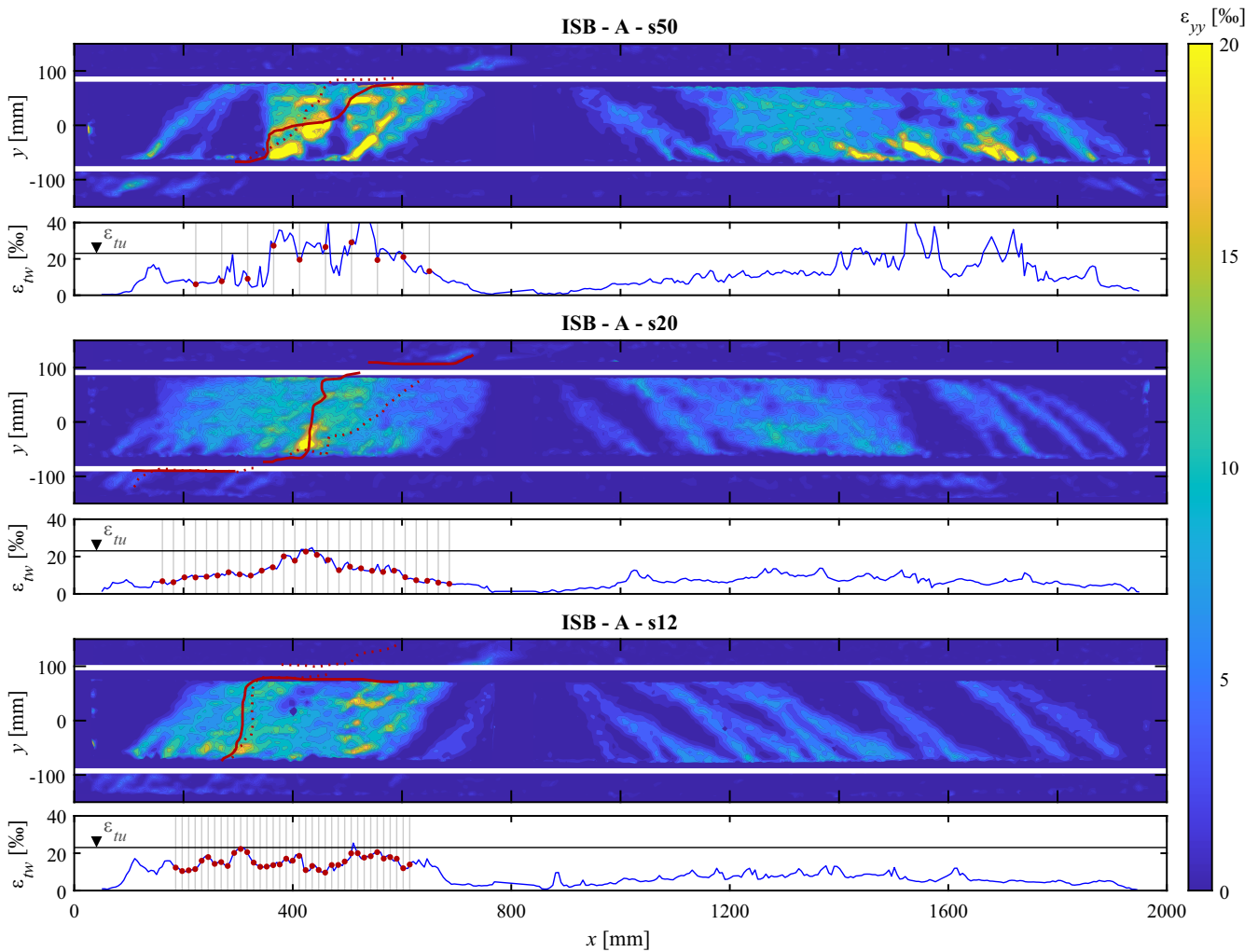
FIGURE 9 Full field strain measurements in direction of aramid inlays (ε_{yy}) and maximum strains (ε_{tw}) along the beams, with the gray lines denoting the inlays crossing the governing crack in the concrete, the red dots denoting the representative strains in the rovings considered for the textile contribution, and the red solid and dotted lines denoting the failure crack in the textile on the front and back side of the specimen, respectively.
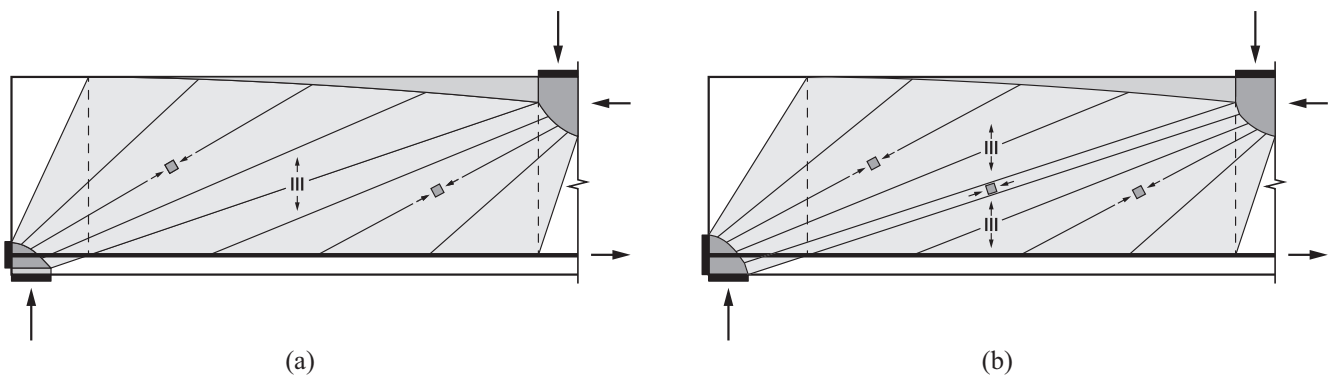

FIGURE 10 Load suspension mechanism in beams under point load: (a) pure fan action; (b) combined fan and direct strut.

carried across the governing crack by the textile reinforcement in the initial loading cycle, which is considerably smaller than the measured load at failure observed

in the experiments for lower amounts of high-strength inlays but correlates well for higher transverse reinforcement ratios. The difference between the ultimate shear
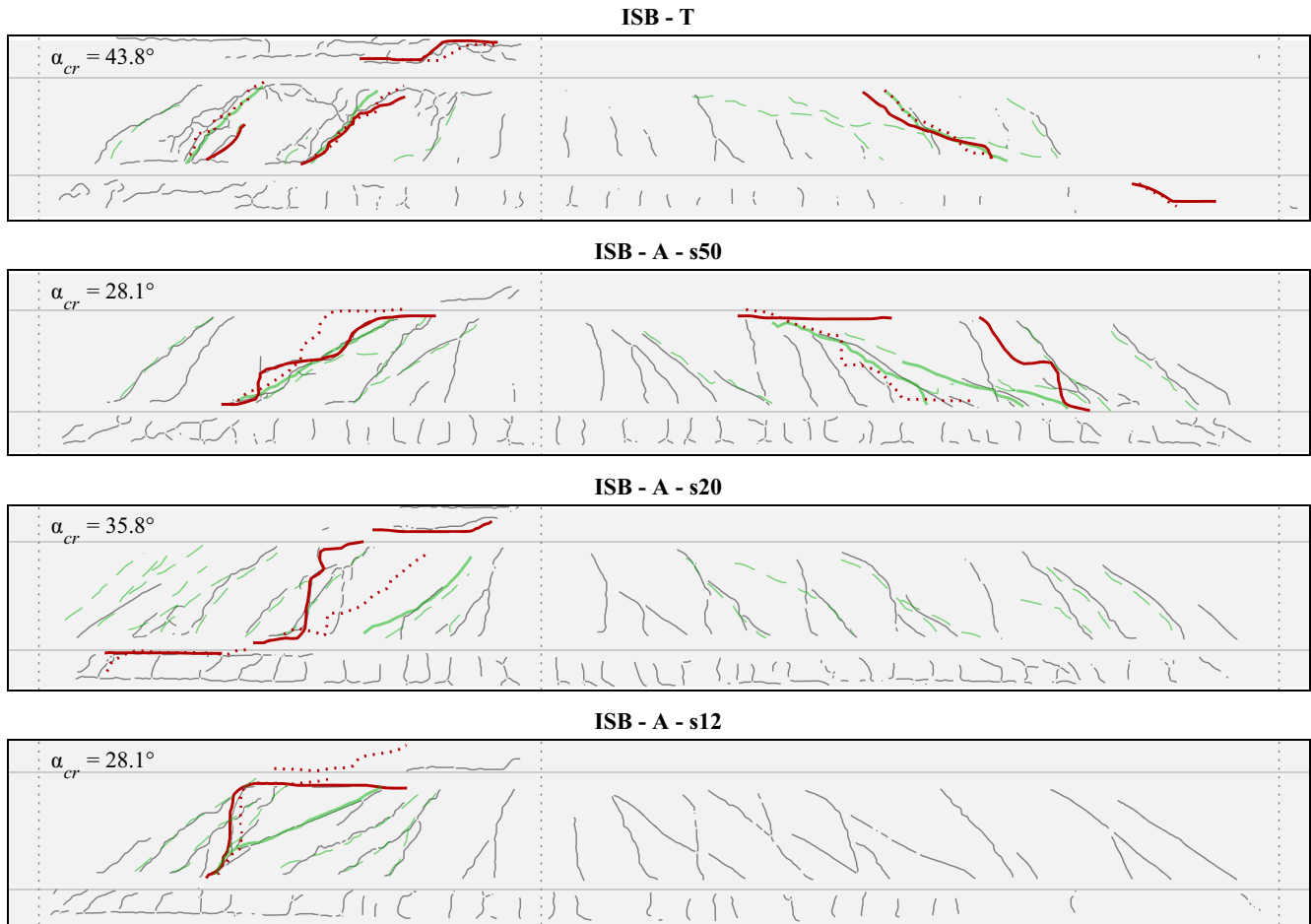
FIGURE 11 Crack patterns in the textile detected with digital image correlation and Automated Crack Detection and Measurement (gray lines), failure cracks in the textile (red lines), and cracks in the concrete from visual inspection after testing (green solid and dashed lines denoting governing and secondary cracks, respectively) with average inclination of governing crack (α_{cr}).
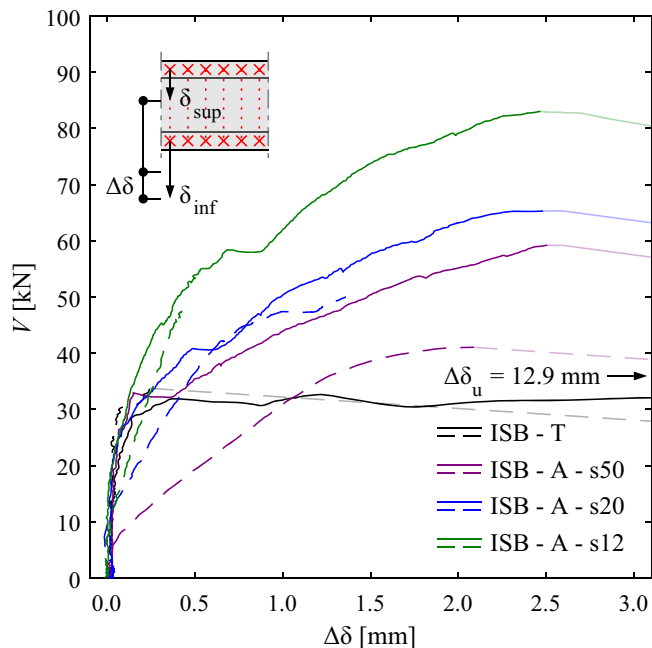
FIGURE 12 Shear force (V) versus maximum vertical component of shear crack opening ($\Delta\delta$).

force in the experiment and the measured contribution from the textile reinforcement crossing the crack can be explained by flatter inclinations of the compressive stresses in the web, enabled by aggregate interlock in the steeper cracks, as well as direct strut action, as illustrated in Figure 10b.

The utilization of the aramid rovings, i.e., the forces carried by the textile reinforcement measured with DIC ($V_{tw,exp}$) divided by the nominal shear strength ($V_{tw,nom}$), setting $\varepsilon_{tw,i} = f_{tu}$ in Equation (1), was between 50% and 66%, showing that the full tensile capacity of the transverse textile reinforcement could not be exploited. Note, however, that only the measurements from the front side of the specimens were available. The maximum strains in the textile reinforcement are dependent on the degree of debonding, which may slightly differ on either side of the web, as highlighted in Ref. [18]. Considering the utilization of the roving strength, discontinuous stress fields with a reduced tensile strength of the textile reinforcement may present a simple design approach to estimate the shear resistance, as proposed in Refs. [2,20].
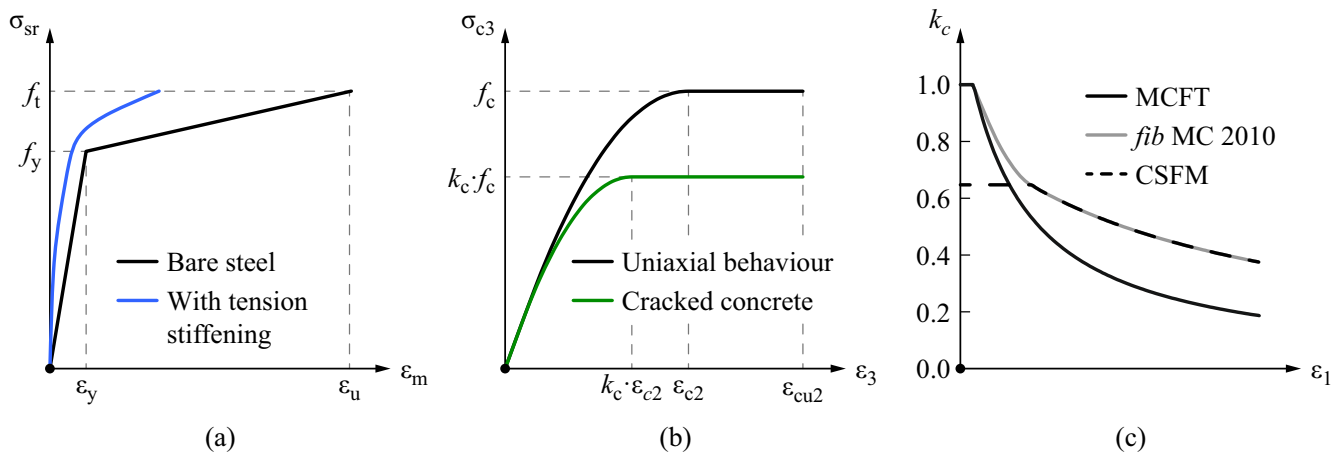
FIGURE 13 Modeling of constitutive laws in Compatible Stress Field Method: (a) tension stiffening effect in reinforcement, (b) compression softening in concrete, (c) compression softening law. MCFT, modified compression field theory.

However, more experiments with various transverse reinforcement ratios and shear slendernesses are necessary for the calibration of the reduction factors.

4.4 | Crack behavior

The assessment of the crack pattern and kinematics was not directly possible from the displacement and strain measurements on the surfaces of the specimens, as described in Section 4.3. The cracks in the concrete were located after testing (both loading cycles) by stripping off the formwork and determining the crack patterns from visual inspection, as illustrated in Figure 5f, which only allowed the detection of the major shear cracks since most of the bending cracks were not recognizable by eye after unloading. Figure 11 shows the combined crack patterns of the textile (gray lines), the failure cracks in the textile (red solid and dotted lines, denoting the front and back side, respectively), and the cracks in the concrete (green solid and dashed lines, denoting the governing and secondary cracks, respectively). Note that the illustrated crack patterns are the result of both the initial and reloading cycle. All specimens exhibited the formation of multiple diagonal cracks in the web. While the initial cracks with an inclination of ~45° coincided well between the textile and the concrete, the cracks with flatter inclination—which formed at higher load levels—and specifically the governing shear crack (denoted as a bold green line, with the average inclination α_{cr} indicated in Figure 11) were often not detected in the crack pattern in the textile determined with ACDM. The locations of the failure cracks in the textile were generally not identical to the cracks in the concrete and also differed between the front and the back sides of the specimens.

While there were no direct measurements of the crack opening and slip available, a valid approach to

estimate the shear crack opening consists in measuring the relative deflections of the top and bottom chord of the concrete beam, as described in Ref. [18]. Figure 12 shows the shear force in the governing span (V) against the maximum vertical component of the shear crack opening ($\Delta\delta$). The shear cracks started opening within a close range of the applied shear force in all specimens under initial loading, whereby the subsequent load increase was dependent on the inlay spacing. All specimens with transverse textile reinforcement exhibited a similar crack opening at failure in the initial loading cycle. However, the governing crack in Specimen "ISB-T" grew to a considerably higher opening without increasing the load, supporting the hypothesis of substantial crack sliding as described in Sections 4.1 and 4.2, while the reloading cycle and the failure in the longer shear span occurred at a small crack opening, as expected in concrete beams without transverse reinforcement. The shear force-crack opening relationships of the specimens that failed due to concrete crushing in flexure ("ISB-A-s20" and "ISB-A-s12") followed relatively closely with the curve obtained under initial loading. However, Specimen "ISB-A-s50" displayed the opening of the governing shear crack at much lower load levels, suggesting that a substantial shear crack had already formed under initial loading, which presumably had caused the lower failure load in the reloading cycle.

5 | NUMERICAL MODELING BASED ON COMPATIBLE STRESS FIELD METHOD

The load–deformation and the failure behavior of the thin-walled concrete beams were examined using the commercial software "IDEA StatiCa Detail,"[34] which
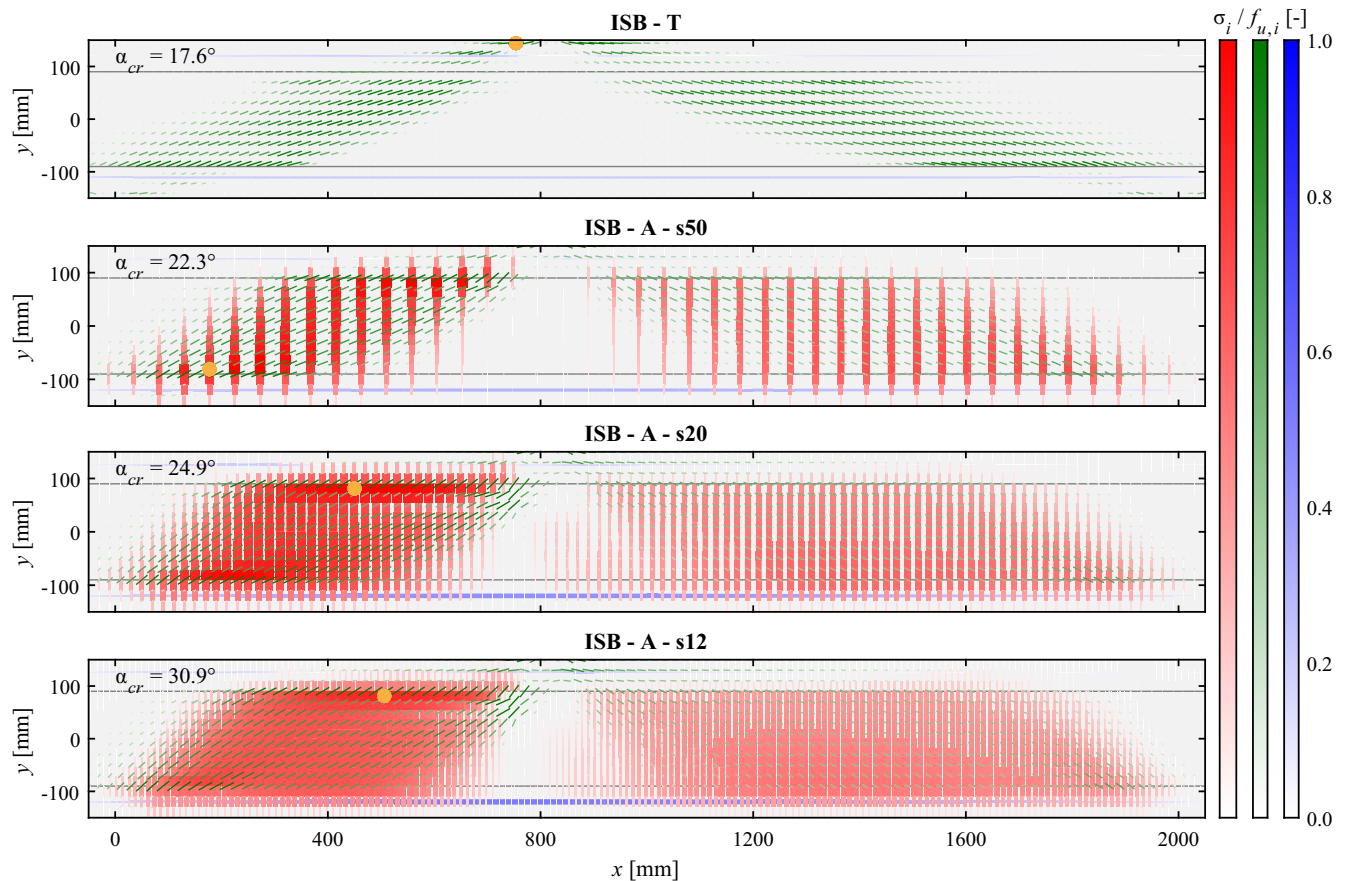
FIGURE 14 Utilizations (stress divided by effective strength, admissible stress, and yield strength, respectively) predicted with compatible stress fields for transverse aramid rovings (red), concrete (green, inclinations of lines according to principal direction), and deformed steel bars (blue), with thicknesses of reinforcement and line lengths of compressive stresses proportional to their magnitudes, and yellow dots denoting governing element (utilization = 1).

was developed in a collaboration of the Institute of Structural Engineering (ETH Zurich) and the software company IDEA RS. The applied method consists of continuous stress fields based on a nonlinear finite element analysis ("Compatible Stress Field Method" [CSFM]),[35] which considers simple uniaxial constitutive laws for concrete and reinforcement and automatically yields the effective compressive strength of the concrete. A similar approach based on elastic-cracked stress fields was successfully applied by Valeri et al.[2] to thin-walled concrete beams with conventional textile reinforcement in bending. Besides the strain compatibility, the consideration of tension stiffening is unique to the methodology presented in this study, making it particularly suitable for investigating the behavior of concrete structures with brittle reinforcement materials since their strength is essentially dependent on the deformation state, and methods based on limit analysis (e.g., discontinuous stress fields) are generally not applicable due to the lack of ductility, and the related insufficient deformation capacity.

5.1 | Main assumptions

The CSFM models the response of reinforced concrete elements under in-plane loading by assuming fictitious, rotating, stress-free cracks, where the principal directions of stresses and strains coincide. The tensile strength of the concrete is neglected, except for its tension stiffening effect, which allows capturing the mean strains in the reinforcement (ε_m), as shown in Figure 13a. Tension stiffening is implemented by modifying the stress–strain relationship of the bare reinforcing bars to consider the average stiffness of a bar due to its interaction with the concrete, where the effective area activated in tension is calculated based on the geometric layout of the reinforcing bars in the tension chord (for a more detailed description, see Ref. [34]). The constitutive law of concrete follows the parabola-rectangle diagram of EN1992-1-1,[36] and its strength is adjusted according to the compression softening effect for cracked concrete based on the principal tensile strain (ε_1) using the k_c reduction factor, illustrated in Figure 13b,c. This

constitutive behavior corresponds to a level-of-approximation IV according to the classification framework for stress fields and strut-and-tie models proposed in the *fib* Bulletin 100.[37] Despite the simplicity of the model assumptions, the evaluation of the response in the concrete and reinforcement using uniaxial laws has proven to yield accurate predictions of the global load–deformation behavior and the bearing capacity for reinforced concrete members.[34] However, the analysis of concrete elements without transverse reinforcement needs to be treated with more caution since the shear transfer across cracks typically relies on other contributions from the concrete, such as aggregate interlock or residual tensile stresses in the fracture process zone, which are not considered in CSFM.

5.2 | Model parameters

The specimens were modeled as I-profile sections with the nominal dimensions, as specified in Figure 3, neglecting the presence of the GFRP rods and the nonstructural base textile. The compressive strength and Young's modulus were defined for each specimen according to the material tests presented in Section 3.1.4. The aramid rovings were modeled as closed stirrups with zero concrete cover and different spacings, according to Table 1. The software only allows for a minimum reinforcing bar diameter of 1 mm. Therefore, the material properties of the transverse reinforcement were adjusted to provide the same strength and axial stiffness of the rovings, as presented in Section 3.1.1, leading to equivalent values for the tensile strength and Young's modulus of 1827 MPa and 79.2 GPa, respectively, implemented in a linear elastic stress–strain relationship (brittle failure with no ductility). The reinforcing bars were modeled as straight bars with a bi-linear constitutive law where the material properties were defined following Table 2. The tension stiffening effect was considered using the default parameters for determining the effective concrete area activated in tension. All partial safety factors were set to one. The load was incrementally increased until the ultimate load was reached.

5.3 | Results from simulation and comparison to experimental results

The predictions using CSFM were validated with the experimental results regarding their global load–deformation behavior, the ultimate load, and the failure modes. The load–deflection relationships denoted as red curves in Figure 4 generally compared well with the

tested beams. The postcracking stiffness of Specimen "ISB-T" was underestimated, and the simulation did not capture the distinct crack sliding prior to failure. While the load–deflection curve of Specimens "ISB-A-s20" and "ISB-A-s12" exhibited good agreement in the initial postcracking phase, the flexural stiffness slightly decreased in the experiments once the governing shear crack started forming (as described in Section 4.4 and shown in Figure 12), which did not occur in the CSFM simulations as the postcracking stiffness was fairly linear and only decreased shortly prior to failure. The shear forces at failure are illustrated in Figure 6 and Table 4, which show an excellent correspondence between the experiments and the model predictions. The largest deviation occurred in Specimen "ISB-A-s50" (17%), which, however, was on the conservative side. Figure 14 shows the utilizations of the textile (red) and steel (blue) reinforcement and the concrete (green), with the location of the maximum value (i.e., utilization = 1) marked as yellow dots. While the reinforcement carried the forces in the directions of their axes, the principal directions of the stresses in the concrete are denoted as the inclinations of the plotted lines, which can be interpreted as the representation of the stress fields transferring the loads within the beams. All specimens with high-strength inlays exhibited the failure in the textile reinforcement at the interface between the web and either the top or bottom flange, which agrees well with the observations in the experiments, where the failure crack in the textile was initiated in one roving and propagated over the height of the web and along the web–flange interface, as described in Sections 4.1 and 4.3. The stresses in the rovings did not exhibit distinct peaks but were fairly uniform over the entire height of the beam due to the small contact area between the concrete and the roving (resulting from the small circumference of the roving and the modeling of zero concrete cover, as described in Section 5.2), leading to a limited stress transfer. The inclinations of the principal stresses—which coincide with the cracks, as described in Section 5.1—corresponded well to the experimental results, lying in a similar range around 25°–30°, as shown in Figure 11.

The predicted load transfer of Specimen "ISB-T" without high-strength inlays (shown in Figure 14) mainly depended on the formation of a direct strut from the load introduction to the support, which is reflected by a flat inclination of the compressive stresses. Clearly, the model assumption of stress-free, rotating cracks differs from the actual behavior due to the absence of transverse reinforcement, as observed in the experiment, where the governing shear crack exhibited a steeper inclination and hardly any flatter cracks formed. The failure eventually

occurred in the compression zone in the top flange. While the model provided a reasonable prediction of the load–deflection relationship and an excellent agreement of the ultimate load, one should keep in mind that CSFM does not consider the shear transfer mechanisms that are typically governing in concrete beams without transverse reinforcement (as described in Section 5.1), and the results may differ for other geometrical configurations.

6 | CONCLUSIONS

This study investigated the potential of stay-in-place flexible formworks with integrated transverse textile reinforcement for thin-walled concrete beams. The production of the fabrics using a CNC flat-bed knitting machine allowed the introduction of spatial features to integrate continuous rovings and guide shaping elements within the textile, which led to the development of a novel formwork and reinforcement system. The manufacturing procedure was validated in an experimental campaign consisting of four concrete beams with I-profile cross-sections tested in three-point bending to assess their structural performance. The transverse reinforcement was integrated into the flexible formworks by means of high-strength aramid rovings winding around the deformed steel bars in the top and bottom flanges to ensure proper anchorage.

The experimental results revealed a beneficial post-cracking behavior, with the shear resistance being essentially dependent on the amount of transverse reinforcement. All specimens failed due to the formation of a shear crack and the rupture of the textile reinforcement (where present) under initial loading. After externally reinforcing the beam in the broken shear span, the specimens were subjected to another loading cycle, which led to ambiguous results since the degree of damage during the first loading cycle could not be sufficiently assessed.

The transverse reinforcement ratio proved to be the major parameter in increasing the shear strength. The presence of the textile on the outer surface of the specimens allowed directly assessing the stresses in the shear reinforcement based on DIC deformation measurements. The low bond shear stresses between the textile and the concrete, which solely rely on adhesion and friction, led to a substantial debonding of the transverse reinforcement at high load levels, spreading the strains over the entire depth of the web and effectively reducing the peak strain values in the vicinity of the cracks. However, the full tensile capacity of the aramid rovings crossing the governing crack could not be exploited due to the brittle material behavior, which led to a progressive failure once the first roving reached its tensile

strength. While the observed failure modes were brittle, the combination of high-strength textiles as shear and deformed steel bars as flexural reinforcement promises a benign failure behavior if the transverse reinforcement is designed such that it can sustain the shear forces until a bending failure is reached, as highlighted in a previous study by the authors on concrete beams with rectangular cross sections.[18]

The CSFM, based on a finite element analysis assuming fictitious, rotating, stress-free cracks, was used to predict the load-deformation and failure behavior of the tested specimen. Due to the consideration of the strain compatibility and the tensioning stiffening effect, this method is particularly suitable for modeling concrete structures with brittle reinforcement materials since their strength is essentially dependent on the deformations. The model predictions yielded an excellent agreement between the applied shear at failure and the experimental values for the specimens with high-strength inlays, even providing the inclinations of the governing cracks. The methodology based on compatible stress fields, thus, presents a valid approach for the design of the transverse textile reinforcement in thin-walled concrete beams to achieve a ductile failure behavior in bending. While the predicted ultimate load of the specimen without transverse reinforcement also corresponded well with the experimental value, the model did not capture the observed large deformations prior to failure, which is attributed to crack sliding.

In this study, a novel type of stay-in-place flexible formworks with integrated transverse textile reinforcement is introduced, which offers many possibilities for a material-efficient design of concrete structures. The use of weft-knitted textiles allows the further optimization of the elements, including the variation of the depth of the cross section and the inlay spacing along the length of the beam, which may be the subject of future research. However, the placement of the textile reinforcement on the exterior of the elements due to its use as stay-in-place flexible formworks presents challenges regarding its behavior under fire due to the direct exposure to the environment and the relatively low glass transition temperature of epoxy resins typically used as coating, which require further examinations.

AUTHOR CONTRIBUTIONS

Minu Lee: Conceptualization, methodology, investigation, visualization, and writing – original draft. **Jaime Mata-Falcón:** Conceptualization, methodology, writing – review & editing, and supervision. **Mariana Popescu:** Methodology, writing – original draft (Section 3.1.1), review & editing. **Walter Kaufmann:** Conceptualization, writing – review & editing, and funding acquisition.

ACKNOWLEDGMENTS

CONFLICT OF INTEREST STATEMENT

The authors declare that they have no known competing financial interests or personal relationships that could have appeared to influence the work reported in this paper.

DATA AVAILABILITY STATEMENT

The data that support the findings of this study are openly available in ETH Research Collection at https://www.research-collection.ethz.ch/handle/20.500.11850/555795, reference number 10.3929/ethz-b-000555795.

ORCID

Minu Lee https://orcid.org/0000-0002-6489-8310
Jaime Mata-Falcón https://orcid.org/0000-0001-8701-4410
Walter Kaufmann https://orcid.org/0000-0002-8415-4896

REFERENCES

1. Kromoser B, Preinstorfer P, Kollegger J. Building lightweight structures with carbon-fiber-reinforced polymer-reinforced ultra-high-performance concrete: research approach, construction materials, and conceptual design of three building components. Structural Concrete. 2019;20:730–44. https://doi.org/10.1002/suco.201700225

2. Valeri P, Ruiz MF, Muttoni A. Modelling of textile reinforced concrete in bending and shear with elastic-cracked stress fields. Eng Struct. 2020;215:110664. https://doi.org/10.1016/j.engstruct.2020.110664

3. Bielak J, Schmidt M, Hegger J, Jesse F. Structural behavior of large-scale I-beams with combined textile and CFRP reinforcement. Appl Sci. 2020;10:4625. https://doi.org/10.3390/app10134625

4. Peled A, Mobasher B, Bentur A. Textile reinforced concrete. Boca Raton, FL: CRC Press, Taylor & Francis Group; 2017.

5. Hegger J, Voss S. Investigations on the bearing behaviour and application potential of textile reinforced concrete. Eng Struct. 2008;30:2050–6. https://doi.org/10.1016/j.engstruct.2008.01.006

6. Valeri P, Fernàndez Ruiz M, Muttoni A. Tensile response of textile reinforced concrete. Construct Build Mater. 2020;258:119517. https://doi.org/10.1016/j.conbuildmat.2020.119517

7. Veenendaal D, West M, Block P. History and overview of fabric formwork: using fabrics for concrete casting. Struct Concr. 2011;12:164–77. https://doi.org/10.1002/suco.201100014

8. Hawkins WJ, Herrmann M, Ibell TJ, Kromoser B, Michaelski A, Orr JJ, et al. Flexible formwork technologies - a state of the art review. Struct Concr. 2016;17:911–35. https://doi.org/10.1002/suco.201600117

9. Orr JJ, Darby A, Ibell TJ, Evernden M, Otlet M. Concrete structures using fabric formwork. Struct Eng. 2017;89:20–6. https://doi.org/10.17863/cam.17019

10. Kostova K, Ibell T, Darby A, Evernden M. Form-finding approach for flexibly formed concrete elements. Proc Inst Civ Eng Eng Comput Mech. 2019;172:96–105. https://doi.org/10.1680/jencm.19.00005

11. Popescu M, Reiter L, Liew A, Van Mele T, Flatt RJ, Block P. Building in concrete with an ultra-lightweight knitted stay-in-place formwork: prototype of a concrete Shell bridge. Structure. 2018;14:322–32. https://doi.org/10.1016/j.istruc.2018.03.001

12. Popescu MA. KnitCrete: stay-in-place knitted formworks for complex concrete structures. Zurich: ETH Zurich; 2019. https://doi.org/10.3929/ETHZ-B-000408640

13. Popescu M, Rippmann M, Liew A, Reiter L, Flatt RJ, Van Mele T, et al. Structural design, digital fabrication and construction of the cable-net and knitted formwork of the KnitCandela concrete shell. Structure. 2020;31:1287–99. https://doi.org/10.1016/j.istruc.2020.02.013

14. Lee M, Mata-Falcón J, Kaufmann W. Load-deformation behaviour of weft-knitted textile reinforced concrete in uniaxial tension. Mater Struct. 2021;54:210. https://doi.org/10.1617/s11527-021-01797-5

15. Lee M, Mata-Falcón J, Kaufmann W. Analysis of the tension chord in the flexural response of concrete elements: methodology and application to weft-knitted textile reinforcement. Eng Struct. 2022;261:261. https://doi.org/10.1016/j.engstruct.2022.114270

16. Lee M, Mata-Falcón J, Kaufmann W. Influence of short glass fibres and spatial features on the mechanical behaviour of weft-knitted textile reinforced concrete elements in bending. Construct Build Mater. 2022;344:128167. https://doi.org/10.1016/j.conbuildmat.2022.128167

17. Lee M, Mata-Falcón J, Popescu M, Block P, Kaufmann W. Potential approaches for reinforcing complex concrete structures with integrated flexible formwork. In: Bos FP, Lucas SS, Wolfs RJM, Salet TAM, editors. Second RILEM international conference on concrete and digital fabrication. Volume 28. Cham: Springer International Publishing; 2020. p. 669–79. https://doi.org/10.1007/978-3-030-49916-7_67

18. Lee M, Mata-Falcón J, Kaufmann W. Shear strength of concrete beams using stay-in-place flexible formworks with integrated transverse textile reinforcement. Eng Struct. 2022;271:114970. https://doi.org/10.1016/j.engstruct.2022.114970

19. Fernàndez Ruiz M, Muttoni A. Building in a lighter and more sustainable manner: textile reinforced concrete for thin structural elements. Cemsuisse Technical Report. Nr. 201407. Lausanne, Switzerland. 2017.

20. Preinstorfer P, Huber P, Huber T, Kromoser B, Kollegger J. Experimental investigation and analytical modelling of shear strength of thin walled textile-reinforced UHPC beams. Eng Struct. 2021;231:111735. https://doi.org/10.1016/j.engstruct.2020.111735

21. Rempel S, Ricker M, Hegger J. Safety concept for textile-reinforced concrete structures with bending load. Appl Sci. 2020;10:7328. https://doi.org/10.3390/app10207328

22. Yu Q, Valeri P, Fernández Ruiz M, Muttoni A. A consistent safety format and design approach for brittle systems and application to textile reinforced concrete structures. Eng Struct. 2021;249:113306. https://doi.org/10.1016/j.engstruct.2021.113306

23. Preinstorfer P, Kromoser B, Kollegger J. Flexural behaviour of filigree slab elements made of carbon reinforced UHPC. Construct Build Mater. 2019;199:416–23. https://doi.org/10.1016/j.conbuildmat.2018.12.027

24. Burger J, Lloret-Fritschi E, Scotto F, Demoulin T, Gebhard L, Mata-Falcón J, et al. Eggshell: ultra-thin three-dimensional printed formwork for concrete structures. 3D Print Addit Manuf. 2020;7:48–59. https://doi.org/10.1089/3dp.2019.0197

25. Lloret-Fritschi E, Wangler T, Gebhard L, Mata-Falcón J, Mantellato S, Scotto F, et al. From smart dynamic casting to a growing family of digital casting systems. Cem Concr Res. 2020;134:106071. https://doi.org/10.1016/j.cemconres.2020.106071

26. R&G Faserverbundwerkstoffe GmbH. Technische Daten - Epoxydharz L. 2020.

27. Marti P. Size effect in double-punch tests on concrete cylinders. Mater J. 1989;86:597–601. https://doi.org/10.14359/2261

28. Correlated Solutions. Vic-3D software manual. Irmo: Correlated Solutions; 2019.

29. Fachbereich Prozessmesstechnik und Strukturanalyse. VDI/VDE 2626 Blatt 1 - Optische Messverfahren - Bildkorrelationsverfahren - Grundlagen und Begriffe. VDI/VDE-Gesellschaft Mess- und Automatisierungstechnik. 2018.

30. Mata-Falcón J, Haefliger S, Lee M, Galkovski T, Gehri N. Combined application of distributed fibre optical and digital image correlation measurements to structural concrete experiments. Eng Struct. 2020;225:111309. https://doi.org/10.1016/j.engstruct.2020.111309

31. Gehri N, Mata-Falcón J, Kaufmann W. Automated crack detection and measurement based on digital image correlation. Construct Build Mater. 2020;256:119383. https://doi.org/10.1016/j.conbuildmat.2020.119383

32. Gehri N, Mata-Falcón J, Kaufmann W. Refined extraction of crack characteristics in large-scale concrete experiments based on digital image correlation. Eng Struct. 2022;251:113486. https://doi.org/10.1016/j.engstruct.2021.113486

33. Huber P, Huber T, Kollegger J. Investigation of the shear behavior of RC beams on the basis of measured crack kinematics. Eng Struct. 2016;113:41–58. https://doi.org/10.1016/j.engstruct.2016.01.025

34. Kaufmann W, Mata-Falcón J, Weber M, Galkovski T, Tran DT, Kabelac J, et al. Compatible stress field design of structural concrete: principles and validation. Zurich, Brno: ETH Zurich, Institute of Structural Engineering (IBK); IDEA StatiCa s.r.o.; 2020.

35. Mata-Falcón J, Tran DT, Kaufmann W, Navrátil J. Computer-aided stress field analysis of discontinuity concrete regions. Computational modelling of concrete structures: proceedings of the conference on computational modelling of concrete and concrete structures (EURO-C 2018). 2018, Bad Hofgastein, Austria: CRC Press, pp. 641–50.

36. EN 1992-1-1. Eurocode 2: Design of concrete structures - Part 1-1: general rules and rules for buildings. 2004.

37. Passos Sério Lourenço MF, Fernández Ruiz M, Haugerud SA, Blaauwendraad J, Bousias S, Hoang LC, et al. Fib bulletin 100. Design and assessment with strut-and-tie models and stress fields: from simple calculations to detailed numerical analysis. Fib. The International Federation for Structural Concrete. 2021 https://doi.org/10.35789/fib.BULL.0100

AUTHOR BIOGRAPHIES

Minu Lee, Institute of Structural Engineering, ETH Zurich, Switzerland
Email: mlee@ethz.ch

Jaime Mata-Falcón, Institute of Structural Engineering, ETH Zurich, Switzerland
Email: mata-falcon@ibk.baug.ethz.ch

Mariana Popescu, Faculty of Civil Engineering and Geosciences, Delft University of Technology (TU Delft), The Netherlands
Email: M.A.Popescu@tudelft.nl

Walter Kaufmann, Institute of Structural Engineering, ETH Zurich, Switzerland
Email: kaufmann@ibk.baug.ethz.ch